Modelling of sub-wavelength THz sources as Gaussian apertures

Hungyen Lin[1], Christophe Fumeaux[1], Bernd Michael Fischer[1,2] and Derek Abbott[1]

[1]*School of Electrical & Electronic Engineering, The University of Adelaide, SA 5005, Australia*
[2]*Institut Franco-Allemand de Recherches de Saint Louis, BP 70034, 68301 Saint Louis Cedex, France*
hlin@eleceng.adelaide.edu.au

Abstract: The THz emission point on a nonlinear electro-optical crystal for generating broadband THz radiation is modeled as a radiating Gaussian aperture. With the wavelengths of the infrared pump beam being much smaller than the wavelength components of the generated THz pulse, a THz sub-wavelength radiating aperture with Gaussian profile is effectively created. This paper comprehensively investigates Gaussian apertures in focused THz radiation generation in electro-optical crystals and illustrates the breakdown of the paraxial approximation at low THz frequencies. The findings show that the shape of the radiation pattern causes a reduction in detectable THz radiation and hence contributes significantly to low signal-to-noise ratio in THz radiation generation. Whilst we have demonstrated the findings on optical rectification in this paper, the model may apply without a loss of generality to other types of apertures sources in THz radiation generation.

OCIS codes: (110.6795) Terahertz imaging; (300,6495) Spectrocsopy, terahertz.

References and links

1. G. Mourou, C. V. Stancampiano, V. Antonetti, and A. Orszag, "Picosecond microwave pulses generated with a subpicosecond laser-driven semiconductor switch," Appl. Phys. Lett. **39**, 295 - 296 (1981).
2. C. Fattinger, and D. Grischkowsky,"Point source terahertz optics," Appl. Phys. Lett. **53**, 1480 - 1482 (1988).
3. M. Bass, P. A. Franken, J. F. Ward, and G. Weinreich, "Optical rectification," Phys. Rev. Lett. **9**, 446 – 448 (1962).
4. X.-C. Zhang, Y. Jin, and X. F. Ma "Coherent measurement of THz optical rectification from electro-optic crystals," Appl. Phys. Lett. **61**, 2764 – 2766 (1992).
5. A. Rice, Y. Jin, X. Ma, X.-C. Zhang, D. Bliss, J. Larkin, and M. Alexander "Terahertz optical rectification from $\langle 110 \rangle$ zinc-blende crystals," Appl. Phys. Lett. **64**, 1324 – 1326 (1994).
6. Q. Chen, and X.-C. Zhang, "Polarization modulation in optoelectronic generation and detection of terahertz beams," Appl. Phys. Lett. **74**, 3435 – 3437 (1999).
7. T. Yuan, S. P. Mickan, J. Xu, D. Abbott, and X.-C. Zhang "Towards an apertureless electro-optic T-ray microscope," *CLEO*, 637 – 638 (2002).
8. R. Lecaque, S. Gresillon, and C. Boccara, "THz emission Microscopy with sub-wavelength broadband source," Opt. Express **16**, 4731 – 4738 (2008).
9. W. Withayachumnankul, G. M. Png, X. Yin, S. Atakaramians, I. Jones, H. Lin, B. S. Y. Ung, J. Balakrishnan, B. W.-H. Ng, B. Ferguson, S. P. Mickan, B. M. Fischer, and D. Abbott, "T-ray sensing and imaging," Proceedings of the IEEE **95**, 1528 - 1558 (2007).
10. B. E. A. Saleh, and M. C. Teich, *Fundamentals of Photonics* (John Wiley & Sons, 1991).
11. S. J. Orfanidis, *Electromagnetic Waves and Antennas* (http://www.ece.rutgers.edu/ orfanidi/ewa/ch17.pdf, 2008).
12. C. Fumeaux, D. Baumann, S. Atakaramians, and E. Li "Considerations on paraxial Gaussian beam source conditions for time-domain full-wave simulations," *25th Annual Review of Progress in Applied Computational Electromagnetics*, 401 – 406 (2009).

13. J. Xu, and X.-C. Zhang, "Optical rectification in an area with a diameter comparable to or smaller than the center wavelength of terahertz radiation," Opt. Lett. **27,** 1067 – 1069 (1999).
14. G. Dakovski, B. Kubera, and J. Shan "Localized terahertz generation via optical rectification in ZnTe," J. Opt. Soc. Am. B **22,** 1667 – 1670 (2005).
15. Q. Xing, L. Lang, Z. Tian, N. Zhang, S. Li, K. Wang, L. Chai, and Q. Wang, "The effect of two-photon absorption and optical excitation area on the generation of THz radiation," Opt. Commun. **267**, 422 – 426 (2006).
16. T. Hattori, K. Tukamoto, R. Rungsawang, and H. Nakatsuka, "Knife edge measurement of tightly focused tera- hertz pulses," *The 8th International Workshop on Femtosecond Technology*, 1 (2001).
17. C. A. Balanis, *Antenna Theory: Analysis and Design* (John Wiley & Sons, 1997).
18. A. Taflove, and S. C. Hagness, *Computational Electrodynamics: The Finite-Difference Time-Domain Method* (Artech House, 2005).
19. A. Nahata, A. S. Weling, and T. F. Heinz, "A wideband coherent terahertz spectroscopy system using optical rectification and electro-optic sampling," Appl. Phys. Lett. **69**, 2321 – 2323 (1996).
20. X. Xie, J. Xu, J. Dai, and X.-C. Zhang, "Enhancement of terahertz wave generation from laser induced plasma," Appl. Phys. Lett. **90**, 141104 – 141107 (2007).

1. Introduction

Photoconduction [1, 2] and optical rectification are two of the most common approaches for generating broadband, pulsed THz radiation. Optical rectification is a second-order nonlinear effect based on the inverse process of the electro-optic effect [3]. The mechanism relies on an electro-optical crystal with a second order nonlinear coefficient. The temporal THz pulse is given by the second time derivative of the polarisation transient [4]. Practical advice in THz radiation generation is provided in [5, 6]. In our setup, the IR pump beam is generated from Spectra-Physics Mai-Tai pulsed laser and has a beam waist of approximately 1 mm, therefore some degree of optical focusing is necessary for achieving a smaller spot size and a higher generated THz Signal-to-Noise Ratio (SNR). Focusing is also especially required in the case of electro-optical based THz near-field imaging where a small point source with a radial di- mension of only a few microns is desired [7, 8]. Further review on THz near-field imaging techniques can be found in [9].

The Gaussian beam is a solution to the paraxial wave equation and is characterised by a Gaussian intensity distribution in any plane transverse to the direction of propagation [10]. The paraxial approximation is valid for a beam waist w_0 larger than 0.91λ with a divergence angle $\theta_0 < 20°$. For $w_0 < \lambda/5, \theta_0 \rightarrow 90°$, the paraxial theory breaks down and the radiation pattern converges to the well known obliquity factor pattern [11],

$$A_{\mathrm{obl}}(\theta) = \frac{(1+\cos\theta)}{2}. \tag{1}$$

A computational illustration of the transition from paraxial approximation to the obliquity fac- tor with decreasing beam waist can be found in [12]. With the THz wavelengths (100 μm to 3 mm) being orders of magnitude longer than wavelengths in the optical regime (centered around 800 nm), the failing of paraxial theory for THz beams generated from electro-optical crystals pumped by an optical beam becomes increasingly relevant. The dependence of THz radiation on optical excitation size was first studied in a GaAs emitter (500 μm thick) [13] where a de- pendence of the total THz radiation power on the square of the excitation size was observed. This has been further investigated in [14] and it was concluded that for excitation waists smaller than the THz wavelength, THz emission is largely excitation size independent. This last work has been extended for lower pump power in [15]. A higher-order nonlinear process such as two photon absorption is often attributed as the cause behind a reduction in THz radiation throughput in localized THz radiation generation. This paper will consider the problem from a radiating aperture theory perspective, as commonly applied at microwave frequencies. As we will see from the developed numerical model that has been validated by experimental data,

another possible cause in the reduction of power in the lower THz frequency range is that the radiation pattern from the generation crystal is no longer confined to the direction of propagation but rather diffracted widely and dispersed around the crystal leading to a reduction in measurable THz power. The computational model can easily be generalized to work for any optical excitation sizes, distance, and acceptance angle.

2. Experimental far-field beam characterization

A custom THz setup with electro-optical generation and photoconductive antenna detection, as shown in Figure 1, is used in our experiment. Average pump power of 30 mW is used in THz radiation generation with a 1 mm thick $\langle 110 \rangle$ ZnTe crystal from Zomega Terahertz Corporation. The detector is a custom H structure on a LT-GaAs substrate manufactured at the University of Freiburg. Figure 2 shows the THz waveform and spectrum respectively. An approximate SNR of 100 dB and a bandwidth of more than 2.5 THz is achieved. A knife-edge profile measurement similar to [16] is conducted on the THz beam generated from the electro-optical crystal with the knife-edge cutting into the x-axis. A Sheffield steel razor blade is used as the knife-edge.
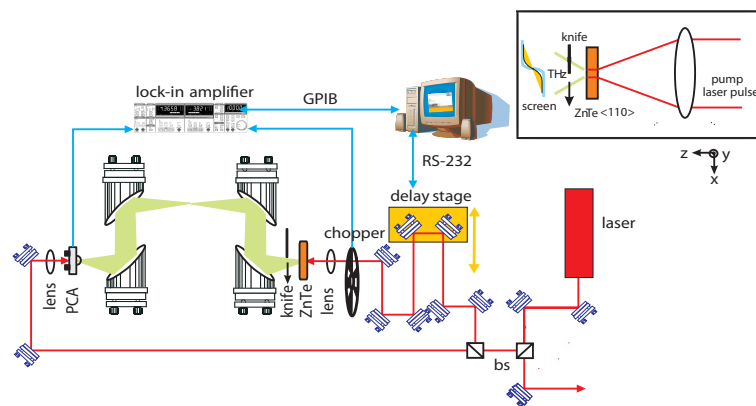

Fig. 1. A THz time domain spectroscopy hybrid setup comprising of a Zomega ZnTe $\langle 110 \rangle$ crystal as emitter and a University of Freiburg, Germany manufactured photoconductive antenna as detector. The inset zooms in on the crystal to knife setup. The pump laser beam is focused into a 1 mm thick ZnTe crystal by means of an optical lens. The emitted THz is sliced along the x-axis by translating a sharp razor blade in the far-field region from the crystal back surface. By doing so, the THz knife-edge profile composed of different frequency components is mapped out.

2.1. IR pump beam waist

To demonstrate the transition of the emitted THz radiation from the obliquity factor diffraction pattern at low frequencies (less than 300 GHz) to a paraxial Gaussian beam at high frequencies (2.5 THz), careful selection of the IR pump laser beam waist is critical as it clearly defines the aperture size. An IR beam waist too small, is unlikely to show a difference between obliquity factor and paraxial theory. Furthermore, prolonged exposure leads to photodamage and hence a reduction in SNR. On the other hand, a pump beam with a large waist will result in a paraxial THz beam for all frequencies. An IR pump beam waist of more than 100 μm is a good trade-off, as 100 μm represents approximately 1.25λ at 2.5 THz, while being $\lambda/5$ at 0.4 THz. We can approximate the IR pump beam waist in our system on the basis of a Gaussian beam propagating through the selected optical components. A further requirement is that the Rayleigh range needs
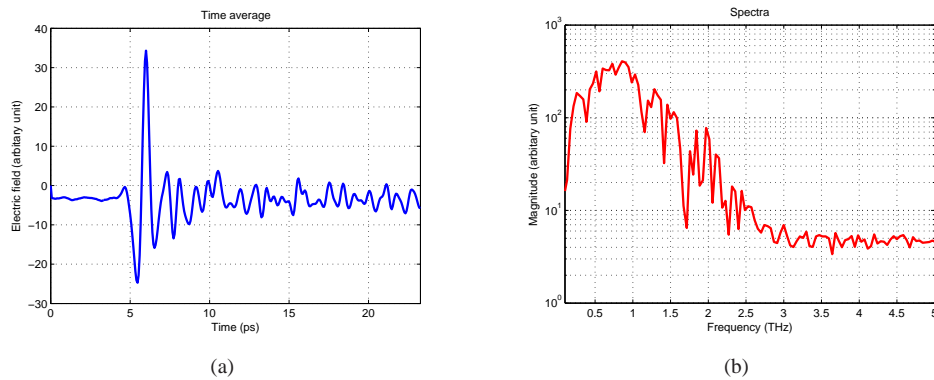
Fig. 2. (a) The THz waveform generated with the THz time domain spectroscopy setup. The time-domain representation is averaged over 10 pulses. (b) Spectrum of the pulse. The setup achieved a SNR of 100 dB and a bandwidth of approximately 3 THz.

to be greater than the crystal thickness to ensure nearly constant beam waist through the crystal. The coherence length of the IR pump beam and THz radiation generated can be found in [19]. A 400 mm focal length optical lens is therefore used resulting in a theoretical IR pump beam waist of 102 μm and Rayleigh range of 41 mm. Taking consideration of beam divergence in crystal, the effective IR pump beam waist is expected to be slightly larger than the theoretical value.

2.2. Crystal to knife-edge distance

In the experiment, the knife-edge is placed in the far-field region from the crystal back surface. As the THz radiation generated is broadband, a worst-case scenario is used in determining the required Fraunhofer distance, i.e. considering shortest THz wavelength. For 2.7 THz, the required sample to crystal surface distance is computed to be 0.75 mm. In the actual experiment, this distance is measured with a CCD camera.

2.3. Crystal to parabolic mirror distance

The THz radiation generated with electro-optical emission is divergent by nature. It is anticipated that when the paraxial theory fails and THz radiation exhibits a diffraction pattern that approaches the obliquity factor, only a limited acceptance angle of the THz beam can be captured by the subsequent parabolic mirror. To increase the acceptance angle, the crystal is displaced closer to the parabolic mirror within the limitation of physical spacing constraint. By doing so, however, the crystal is no longer in the focal length of the parabolic mirror, thereby leading to possible detection issues. Even though experimentally there is no significant difference after optimisation with the detector silicon lens, this is analytically investigated with paraxial theory. It is found that to detect the image with the same position, the detector is required to translate backwards under the same angle of propagation. The distance of translation is simply the distance that the crystal is moved away from the focal length.

3. Beam modelling as radiation from a Gaussian aperture

The electro-optic THz beam generation in the ZnTe crystal is modelled as radiation from an aperture with a Gaussian intensity distribution corresponding to the waist of the IR pump beam. This is justified as THz radiation is coherently generated along the crystal with an IR

pump beam with nearly constant beam waist. Figure 3 presents the framework for modelling. The model initiates with defining a circular area for computation that encloses the Gaussian aperture, but is sufficiently large as to not introduce numerical truncation effects during computation. The computation time, however, scales up quadratically with increasing radius.
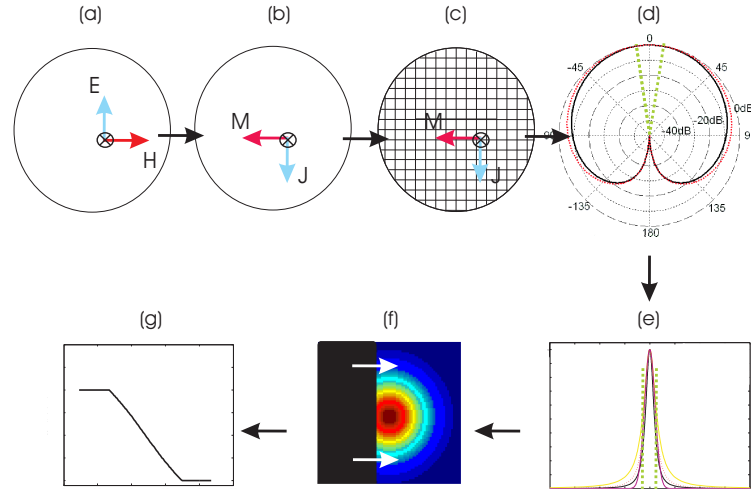

Fig. 3. Main steps to modelling are summarised, clockwise, as follows: (a) Model the THz radiation generation as an aperture with Gaussian intensity distribution and a beam waist identical to that of the IR pump beam. (b) Using the equivalence principle, introduce equivalent electric and magnetic sources in the source aperture. (c) Discretization of the aperture area in a grid. (d) Perform a near-field to far-field transformation, computing the radiation integrals on the basis of the discretized source distribution. (e) Project the far-field intensity distribution on a screen, taking into account the decay of intensity as a function of distance. Truncate the projection at the acceptance angle θ_{win} of the parabolic mirrors. This is highlighted by the green dashed lines. (f) Perform a numerical knife-edge measurement on the field intensity projected on the screen. (g) The resulting curve corresponds to the measured knife-edge intensity profile. It is noted that the sharp truncation of the acceptance angle neglects diffraction effects.

3.1. Equivalent crossed-dipole model

The Gaussian aperture with the intensity distribution of the IR pump beam is applied to a circular THz source surface with normal vector $\hat{n}_s \equiv \hat{z}$ for computational implementation. This can be expressed as phasors for the incident electric and magnetic fields as follows,

$$
\begin{aligned}
E_{i,y} &= E_0 e^{-\frac{r^2}{w_0^2}} \\
H_{i,x} &= -\frac{E_{i,y}}{\eta_0},
\end{aligned}
\tag{2}
$$

where E_0 defines the pulse electric field amplitude, w_0 is the smallest pump beam waist (radius), r is the distance from the z-axis on the aperture and η_0 is free space impedance. The direction of propagation in this context is $+z$ leading to the negative sign for the magnetic field. With the field equivalence principle, the incident $\vec{E}_i$ and $\vec{H}_i$ field can be replaced with

an equivalent problem comprising magnetic and electric current source densities, as classically defined in [17], as follows,

$$\begin{aligned} \vec{M}_S &= -\hat{n}_s \times \vec{E}_i \\ \vec{J}_S &= \hat{n}_s \times \vec{H}_i. \end{aligned} \tag{3}$$

The elementary source element from the excitation aperture is therefore the superposition of two perpendicular infinitesimal magnetic and electric dipoles, both of which, are excited with the same power [12].

3.2. Far-field pattern

The source area, i.e. the Gaussian aperture, is subsequently discretized on a grid in order to compute the radiation integrals [17] as the sum of the contributions from electric and magnetic current sources. The methodology and discrete implementation are described in detail as a frequency-domain near-to-far-field transformation in [18]. The resulting radiation pattern is then projected on a far-field screen, which coincides with the plane where the knife-edge scan is performed. To take into account the path loss from the Gaussian aperture to the location on the screen, the projected pattern needs to be weighted by a $1/r^2$ pattern, which reflects the decay of intensity of a spherical wave with distance. Notice however, due to the nature of a THz Time Domain Spectroscopy (TDS) detection setup, we are unable to map out the entire radiation pattern, i.e. $-90° \leq \theta \leq 90°$. Therefore the green dashed lines in Figure 3(d) indicate the measurable acceptance angle that translates into the screen indicated by dashed lines in Figure 3(e). In order to obtain the integrated power that is observed in the knife-edge experiment, a transformation from a Cartesian to a polar coordinate system is performed as the electric field and magnetic field of the source are rotationally symmetric. With the resulting 2D intensity distribution, it is cumulatively integrated across the columns. To mimic the knife-edge experiment, the model considers a sharp truncation of the measured intensity on the screen because of the limited acceptance angles. This neglects diffraction effects and explains the unphysical discontinuity of the modeled knife-edge curve. Adding a knife-edge diffraction model to the present model would solve this issue, but complicates the present considerations considerably. Our present aim is to gain physical insight via the simplified model, and this can then form the basis of future work for adding further sophistication.

4. Results and discussion

4.1. Experimental results

Fourier transforms of the acquired THz time-domain waveforms are computed and the amplitude at each extracted frequency is plotted against the position of the knife-edge. For the sake of simplicity, only the power spectrum at a certain knife-edge location and the knife-edge of selected frequency components in this study are shown in Figure 4. As experiment is conducted in dry atmosphere, the frequency components are selected to avoid water vapor absorption and achieve high SNR. A running average over only one point has been used to preserve data integrity.

4.2. Model validation

To validate the developed computational beam model from a Gaussian aperture, the model is operated with estimated and measured experimental parameter values such as the (i) IR pump beam waist, (ii) acceptance angle as determined from the crystal-parabolic distance, (iii) distance of projection and (iv) the THz frequency of interest. The exact IR pump beam waist
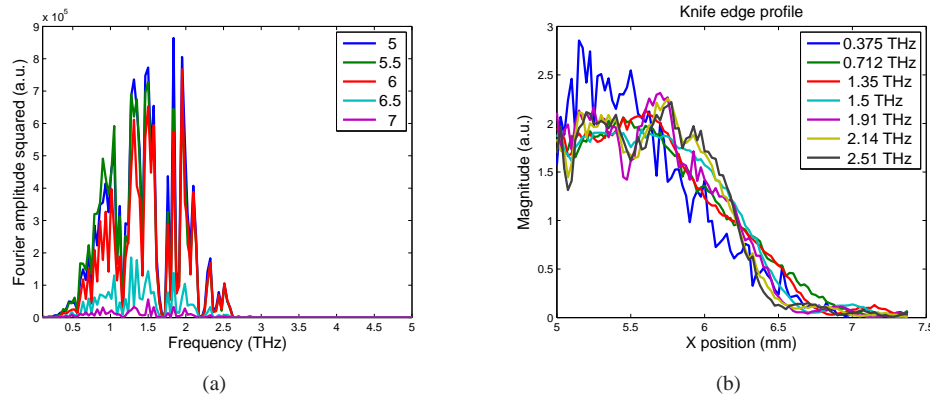
Fig. 4. (a) The power spectrum of the THz waveforms acquired with a knife-edge scanned at a distance of 0.75 mm from the crystal. With each movement of the knife, the THz field becomes weaker until when the THz radiation is entirely blocked by the knife. This can be seen at $x = 5$ mm, where the knife has not obstructed the THz beam, as opposed to $x = 7$ mm, where the THz radiation is totally blocked. (b) Selected frequency components are shown at different knife positions. The knife-edge profile is also shown to illustrate the integrated spatial distribution of the THz pulse at selected frequencies are unaffected by water vapor absorption and noise that occur at high THz frequencies.

inside the crystal is estimated to be greater than 100 μm on the basis of optical alignment. With a relatively thick crystal of 1 mm and the fact that the ZnTe permittivity at IR and THz frequencies are close, we conclude that THz radiation generation is distributed along the bulk crystal thickness. In the model, this distributed generation is approximated as an aperture located at an effective distance within the crystal. Measuring the distance from crystal surface to the knife-edge gives us the range of possible distances for adjusting the effective location and fits the model to the empirical integrated knife-edge function. The criterion for curve fitting is that the free-parameters (beam waist and effective location of the source) are within a realistic range of values, and the resulting knife-edge curves must apply simultaneously to all the selected frequency components. Figures 5 to 11 show the computed normalized radiation patterns and the curve-fitted data for all the selected frequencies, with an IR beam waist in the crystal of 150 μm. To illustrate the goodness of the fit, Figure 12 shows the knife-edge profile at 2.51 THz fitted with the numerical model of 2.51 THz and 0.375 THz respectively. The computed knife-edge function matches closely all the experimental results in terms of the integral function shape and slope. The effect of diffraction is evident in the measured results. Diffraction effect mostly removes the discontinuity in the model and explains the oscillations observed. With the beam waist or aperture size held constant, it is noteworthy to observe the changes in the radiation pattern as the frequency increases. At low frequencies (0.375 THz), the emitted THz pattern resembles the obliquity factor in Equation 1. At frequencies 0.712 and 1.35 THz, the THz beam width begins to approach the paraxial Gaussian beam width. A significant back radiation is also observed in the computational model of the Gaussian aperture. Above those frequencies, the pattern of the THz beam becomes very close the the paraxial Gaussian pattern, as expected.

5. Ramifcations to THz

As we can see from the model, as the IR pump beam waist is very much smaller than the generated longer wavelength components of our THz pulse (e.g. 375 GHz), the THz radiation pattern
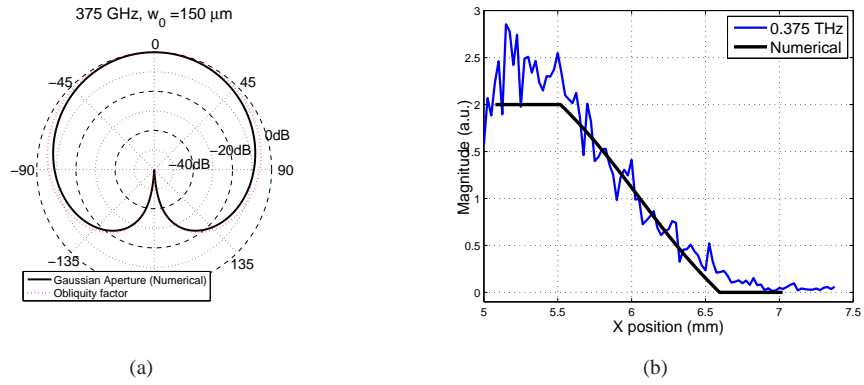
Fig. 5. (a) The radiation pattern and (b) the knife-edge profile at 0.375 THz. The beam waist w_0 is approximately $\lambda/5$ leading to a pattern resembling the obliquity factor.
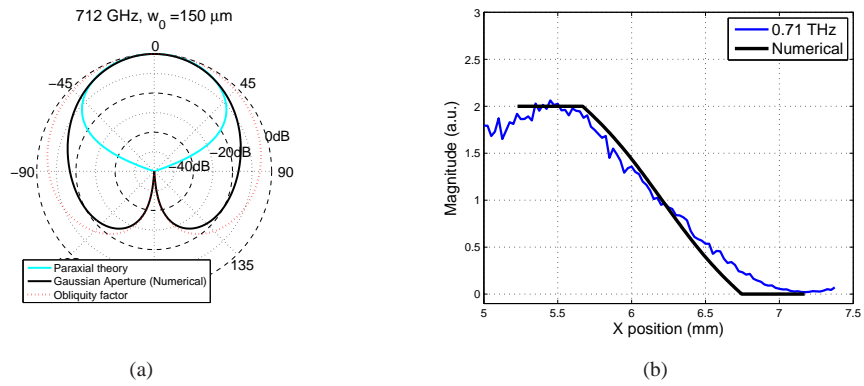

Fig. 6. (a) The radiation pattern and (b) the knife-edge profile at 0.712 THz. The beam waist w_0 is approximately $\lambda/3$ starting to approach paraxial Gaussian beam pattern towards the front.
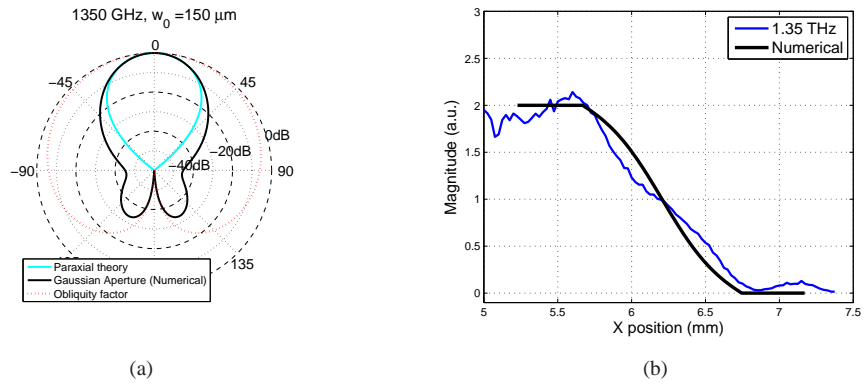

Fig. 7. (a) The radiation pattern and (b) the knife-edge profile at 1.35 THz. The beam waist w_0 is approximately 0.7λ approaching a paraxial Gaussian pattern. Angle of divergence is $27°$.
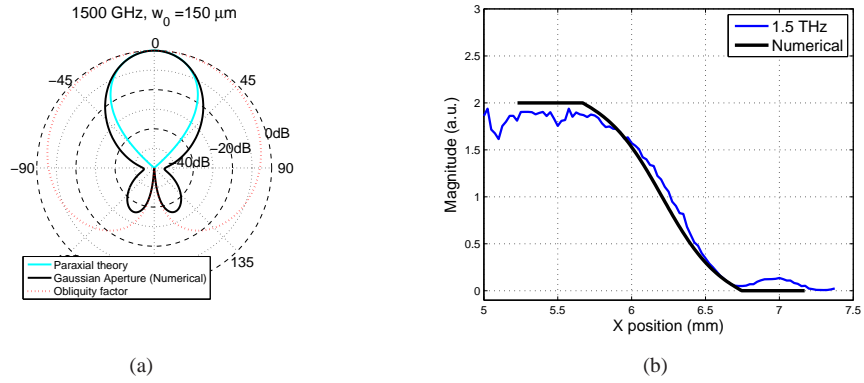
Fig. 8. (a) The radiation pattern and (b) the knife-edge profile at 1.5 THz. The beam waist w_0 is exactly 0.75λ approaching a paraxial Gaussian pattern. Angle of divergence is $24°$.
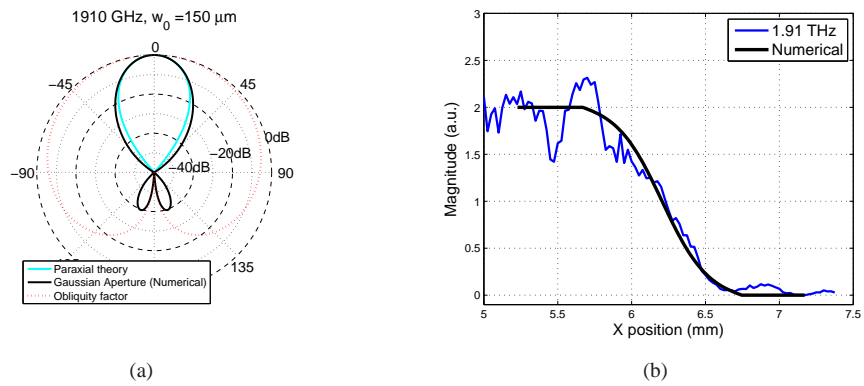

Fig. 9. (a) The radiation pattern and (b) the knife-edge profile at 1.91 THz. The beam waist w_0 is approximately λ approaching a paraxial Gaussian pattern, with the back lobes sightly greater than -40 dB. Angle of divergence is $19°$.
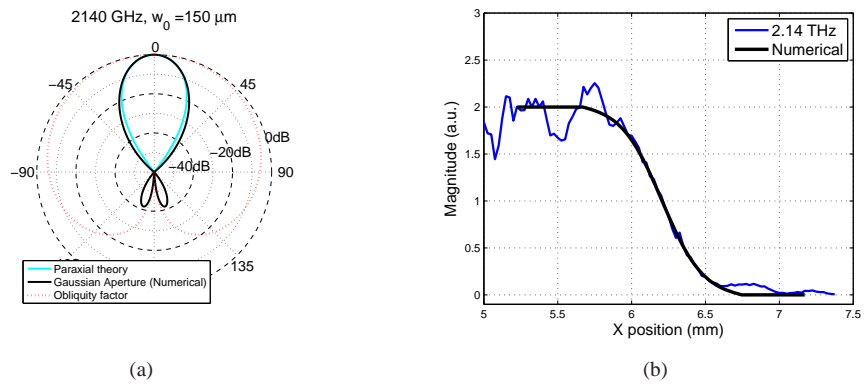

Fig. 10. (a) The radiation pattern and (b) the knife-edge profile at 2.14 THz. The beam waist w_0 is approximately 1.1λ closely resembling the paraxial Gaussian pattern, except for the back lobes less than -40 dB. Angle of divergence is $17°$.
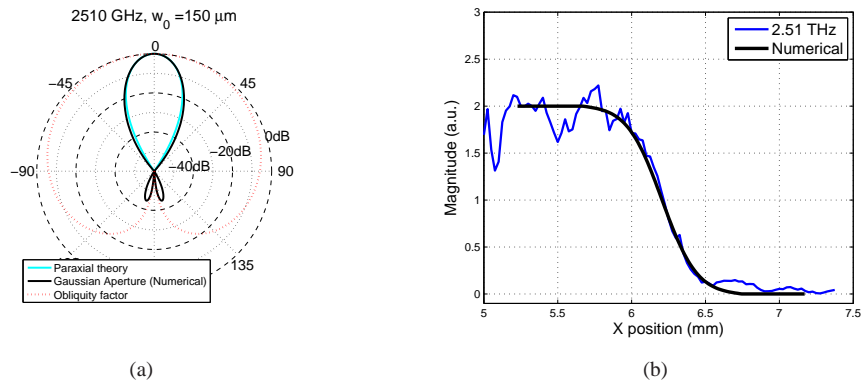
(a)

(b)

Fig. 11. (a) The radiation pattern and (b) the knife-edge profile at 2.51 THz. The beam waist w_0 is approximately 1.25λ closely resembling the paraxial Gaussian pattern, except for the back lobes less than -40 dB. Angle of divergence is $14°$.
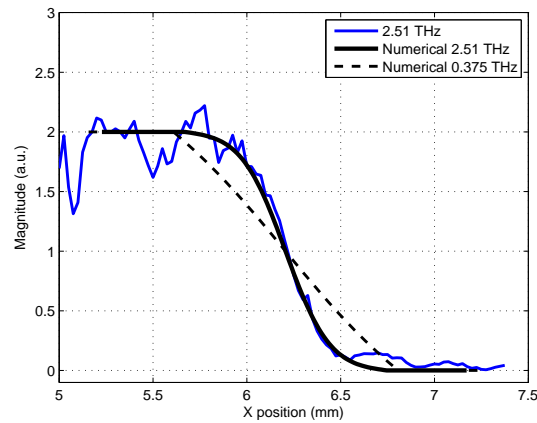

Fig. 12. The goodness of the fit is demonstrated by fitting the knife-edge profile at 2.51 THz with the numerical model of 2.51 THz and 0.375 THz respectively. The latter is chosen to show a distinctive difference between the fits and the validity of the fitting criterion. For curve fitting, the free-parameters (beam waist and effective location of the source) are within a realistic range of values, and the resulting knife-edge curves must apply simultaneously to all the selected frequency components.

becomes nearly independent of the frequency. The THz beam pattern conforms to the obliquity factor and is hence diffracted in all directions around the crystal. Practically this translates into low SNR THz being detected. The result is consistent with the observations reported in [14]. We also can infer from those results that as the IR pump beam waist is increased, the pattern approaches and becomes a paraxial Gaussian beam. With a greater directivity, the SNR of the detected THz increases. The percentage of the detectable power over the total generated power is plotted in Figure 13 against the normalized beam waist w_0/λ for three acceptance angles (10, 20 and 30 degree cones). As expected, at small normalized beam waist, i.e. for IR pump beam waists much smaller than THz wavelengths, the THz radiation is diffracted in all directions leading to little detectable power. As the normalized beam waist increases above one THz, the THz radiation pattern quickly converges to a paraxial Gaussian beam leading progressively to a more directive beam and hence a monotonic increase in detectable power. The curves saturates toward 100% as the divergence angle of the beam decreases below the acceptance angle of detection. Obviously the acceptance angle has an effect on the detectable power and this is governed by the parabolic mirror following the crystal. With a greater acceptance angle, a higher THz power percentage is detectable.
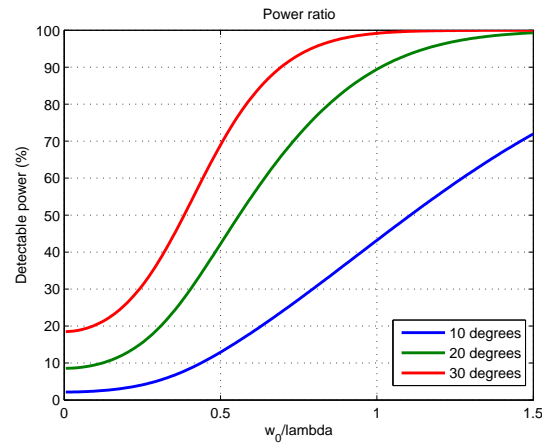

Fig. 13. The detectable THz power percentage over the total generated THz power, with the normalized IR pump beam waist, w_0/λ, on the x-axis for 3 different acceptance angle $\theta_{win} = 10°$, $\theta_{win} = 20°$ and $\theta_{win} = 30°$.

6. Conclusion

In this paper we have model localized THz radiation generation in an ZnTe electro-optical crystal as radiating aperture with Gaussian intensity distribution. We validate the model of Gaussian aperture generation by conducting an experimental knife-edge, taking into account the limitation of THz radiation detection setup. We find that when the IR pump beam waist is very much smaller than the generated THz wavelength, the THz radiation pattern becomes nearly independent of the frequency, conforms to the obliquity factor and is hence diffracted in all directions from the crystal. Practically, this translates into a decreased SNR for the THz radiation reaching the detector. We also demonstrate that as the IR pump beam waist is increased, the pattern approaches and becomes the paraxial Gaussian beam. With a greater directivity, the detected THz SNR increases. As localized THz radiation generation is not only limited to electro-optical crystals, but also holds for photoconductive antennas and plasma generation [20], this work aims

at bringing an awareness to the THz community of the effect of sub-wavelength aperture-like sources in THz radiation generation.